Surface reflectance biases in XCH$_4$ retrievals from the 2.3 μm band are enhanced in the presence of aerosols

Peter Somkuti[1,2], Gregory McGarragh[3], Christopher O'Dell[3], Antonio Di Noia[4,5,6], Leif Vogel[4,5,7], Sean Crowell[8], Lesley Ott[2], and Hartmut Bösch[4,5,6]

[1]Earth System Science Interdisciplinary Center, University of Maryland, College Park, MD, USA
[2]Global Modeling and Assimilation Office, National Aeronautics and Space Administration, Goddard Space Flight Center, Greenbelt, MD, USA
[3]Cooperative Institute for Research in the Atmosphere, Colorado State University, Fort Collins, CO, USA
[4]University of Leicester, Leicester, UK
[5]National Centre for Earth Observation, Leicester, UK
[6]Institute of Environmental Physics (IUP), University of Bremen FB1, Bremen, Germany
[7]now at Kaioa Analytics, Mundaka, Viscay, Spain
[8]LumenUs Scientific, Oklahoma City, OK, USA

Correspondence: Peter Somkuti (peter.somkuti@nasa.gov)

Abstract.

In this work, we present the results of an observing system simulation experiment (OSSE) in which we investigate the emergence of a surface reflectance-dependent bias in retrieved column-averaged dry-air mole fractions of methane (XCH$_4$). Our focus is on single-band type retrievals in the short-wave infrared (SWIR) at 2.3 μm. This particular bias manifests as artificial gradients in XCH$_4$ fields that relate to surface features on the ground and can, for example, cause erroneous estimates of methane source emission rates.

We find that even for near-ideal conditions (that being a perfectly calibrated instrument, perfect knowledge of meteorology and trace gas vertical distributions, and an absence of clouds and aerosols) a surface reflectance-related bias appears in the retrieved XCH$_4$. While the magnitude of the bias is much lower than is observed in e.g. real data from the TROPOspheric Monitoring Instrument (TROPOMI), the overall qualitative shape is strikingly similar. When we study a more realistic scenario by considering synthetic measurements that are affected by aerosols, the surface bias increases in magnitude roughly by a factor of 10. We hold all other properties of the synthetic measurements fixed, and thus can make the following statements about these surface biases from the 2.3 μm absorption band. First, the bias already appears in the near-perfect scenario, meaning that its origin is likely fundamental to XCH$_4$ retrievals from this particular absorption band, and using an optimal estimation-type retrieval approach. Second, the magnitude of the bias increases significantly when aerosols are encountered. As aerosols give rise to a magnification of the bias, we have implemented a retrieval configuration in which the retrieval algorithm knows the true aerosol abundance profiles along with their optical properties. With this configuration, the surface bias returns mostly to the level first seen when synthetic measurements were not affected by aerosols.

The results we present in this work should be considered for new missions where XCH$_4$ is a target quantity and the design relies on the 2.3 μm absorption band. Since the surface bias will likely emerge, it is crucial that a validation approach is planned

which sufficiently samples the needed range of surface reflectance in areas of near-uniform methane concentrations in order to capture the bias and thus correct for it.

1 Introduction

The wealth of data obtained by the TROPOspheric Monitoring Instrument (TROPOMI) very quickly revealed biases in the retrieved trace gases that were hidden until then, since no other trace gas instrument had both spatially dense coverage and footprint sizes on the order of a few square kilometers. Arguably, the most striking one is a bias that strongly correlates with surface reflectance features. Figure 1 shows one example over northeast Africa, in which the described bias is apparent; certain scenes with lower apparent surface reflectance, are accompanied by lower values of column-averaged dry-air methane mole fractions (XCH_4). This clear imprint of surface features onto the XCH_4 fields, driven here mostly by the contrast between rocky and sandy surfaces, is unphysical but routinely dealt with through a post-retrieval bias correction procedure (Hasekamp et al., 2019; Lorente et al., 2021; Schneising et al., 2023).
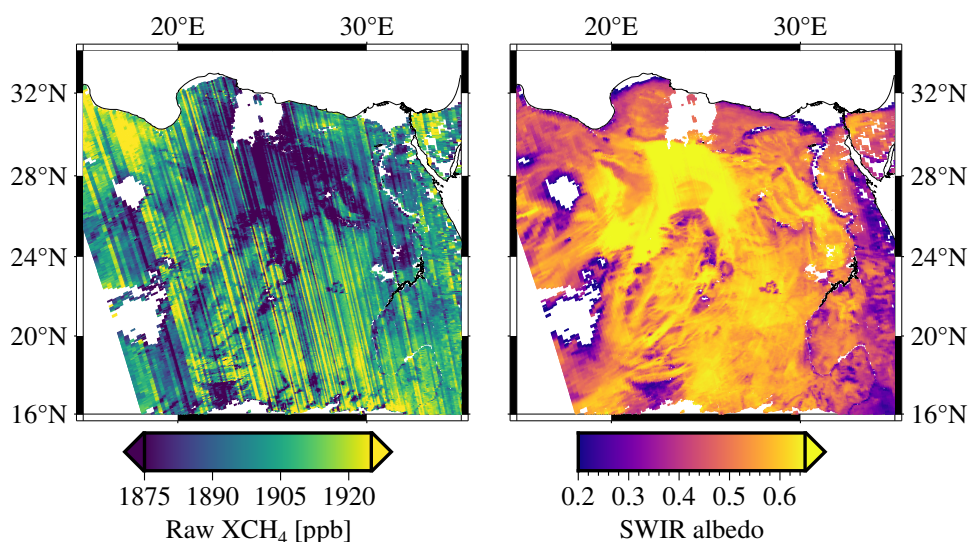

Figure 1. Surface reflectance bias example over northeast Africa. Shown are individual TROPOMI footprints, colored by either raw (without bias correction) retrieved XCH_4 (left) and apparent, retrieved surface albedo (right). Only scenes with albedo larger than 0.2 are shown here. Several surface features (right) are clearly visible to have corresponding gradients in retrieved XCH_4 (left). Colorbar ranges have been adjusted to exaggerate the effect by more strongly pronouncing the image contrast in both panels. No quality filters were applied, this figure is intended to show the raw retrieved methane column before any bias correction. This figure was produced from TROPOMI orbit 27865, processor version 2.4.0 (Copernicus Sentinel-5P, 2021).

As part of the algorithm development efforts for the GeoCarb mission (Polonsky et al., 2014; Moore III et al., 2018; Nivitanont et al., 2019; Somkuti et al., 2021; McGarragh et al., 2024), we investigated the emergence of a surface reflectance bias through a simulation study. We aim to answer questions related to this bias, namely: (1) whether we can reproduce the bias

35   seen in TROPOMI retrievals through simulation-driven retrieval experiments, (2) whether we can determine what drives the emergence of the bias, and, (3) if any mitigation strategy can be employed to reduce it.

    The manuscript is structured in the following way. Section 2 describes the simulation set-up to produce synthetic observations. Section 3 then follows with the description of the retrieval algorithm used to derived the XCH_4 from the simulated radiances. Results are shown and discussed in Section 4, starting with retrievals from aerosol-free simulations (Section 4.1),

40   and then moving on to one with realistic tropospheric aerosol abundances (Section 4.2), where the surface bias is first observed in our study. In Section 4.3 we then augment the retrieval algorithm forward model by including the true aerosol information and analyze its impact on the surface bias. We summarize our results in Section 5 and discuss the both relevance of our study to the real-world biases seen in XCH_4 derived from TROPOMI measurements, as well as mention topics for future investigations.

2   Simulation set-up

45   We use the same tested simulator framework, developed at Colorado State University (O'Brien et al., 2009; Polonsky et al., 2014) that has been successfully applied in other studies, such as Frankenberg et al. (2014); Eldering et al. (2019); Somkuti et al. (2021); McGarragh et al. (2024). Details on the inner workings of this orbit simulator can be found within these mentioned publications; we cover here only a short summary and focus on the aspects that are relevant to our study.

2.1   Sampling

50   Our full simulation set contains scenes derived from real OCO-2 (Crisp et al., 2004; Crisp, 2015) geo-location data within the period of January 2016 until March 2017. Due to the large amount of OCO-2 footprints, which is on the order of one million per day, the geo-location data was down-selected such that only one regular measurement every 10 seconds is retained, ignoring special measurement modes such as target mode. This corresponds to a scaling factor of 240, since OCO-2 measures 8 footprints roughly three times per second. At a global perspective, the general geographical coverage does not change with

55   this down-selection and remains similar to that of the OCO-2 instrument. We retain only nadir-looking (down-looking at the sub-satellite point) scenes and drop any sun-glint following (pointed at the specular reflection of the direct solar beam) viewing modes. For this study, we only consider land surfaces and leave out Antarctica. The coverage of scenes is shown in Fig. 2.

    As Fig. 2 illustrates, our set of scenes contains locations from all land masses with the exception of Antarctica. Since we are sampling MODIS BRDF coefficients (Schaaf and Wang, 2015) at every individual scene location, we obtain surface properties

60   in the proper geographical context for each scene, as captured by the 500m-resolution MCD43A1 product.

2.2   Clouds

We add cloud information from the International Satellite Cloud Climatology Project (ISCCP) by sampling the H-series dataset (Young et al., 2018) at the scene locations and extract cloud flag, cloud type (liquid or ice), cloud path for optical density, and cloud top pressure for the vertical location of the cloud layer. Our measurement simulations fully account for clouds as part

65   of the radiative transfer scheme. For the analysis of the post-retrieval quantities, however, we remove all scenes from the final
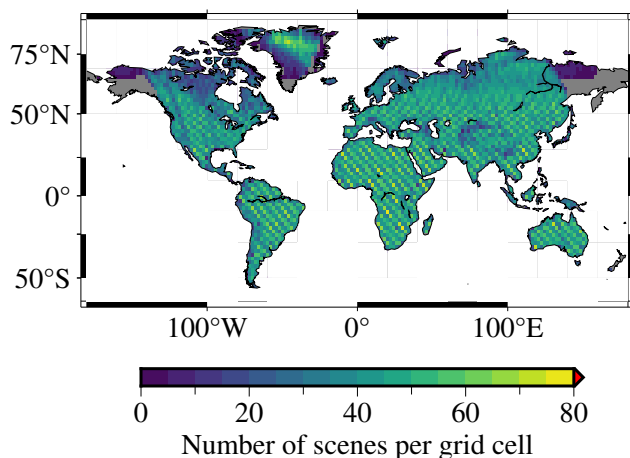
Figure 2. Spatial distribution density of the simulated scenes. Since the simulation locations are based on real OCO-2 locations, the sampling shows the expected striping pattern generated by the orbital movement of the spacecraft. Overall coverage is mostly the same, apart from eastern Siberia and Alaska where OCO-2 measures mostly in glint-mode, which we have excluded from our study. Note that for this and all other global-scale maps, features smaller than 10,000 km^2 in area are not drawn.

analysis that contain any ice or liquid clouds. Our reason behind this choice is that we do not want to exercise cloud flagging algorithms for this work. We show in the following sections that tropospheric aerosols enhance the surface reflectance bias. As such the scene sampling thus becomes representative of a mostly globally distributed set of locations, weighted by the probability of obtaining a cloud-free measurement at those locations and times.

2.3 Aerosols

As in Somkuti et al. (2021), we are utilizing reanalysis data (0.75° spatial and 3-hourly temporal resolution) from the European Centre for Medium-range Weather Forecast's (ECMWF) Copernicus Atmosphere Monitoring System (CAMS) to assign realistic aerosol abundance profiles to each scene (Bozzo et al., 2020). With the CAMS aerosol component, there are in total 11 aerosol mixtures: hydrophobic and hydrophilic organic matter, hydrophobic and hydrophilic black carbon, three sea salt mixtures, three mineral dust mixtures, and sulphate. The sea salt and mineral dust mixtures are separated into three spherical radius size bins each: $0.03 - 0.5\,\mu m$, $0.5 - 5.0\,\mu m$, $5.0 - 20.0\,\mu m$ for sea salt and $0.03 - 0.55\,\mu m$, $0.55 - 0.9\,\mu m$, $0.9 - 20.0\,\mu m$ for mineral dust. The sea salt, sulphate and hydrophilic organic matter mixtures are hygroscopic, meaning that the optical properties and the total aerosol particle counts for a given mass mixing ratio are dependent on the humidity. There is no humidity dependence for the mineral dust, hydrophobic organic matter and black carbon mixtures.

The process of integrating the CAMS model aerosol data into our orbit simulator and then the radiative transfer (RT) module is done as follows. In a pre-processing step, a library of aerosol mixture optical properties is generated according to the micro-physical parameters laid out in Appendix A2 of Bozzo et al. (2020). This step leverages a code for far-field scattering calculations involving polydisperse mixtures of spherical particles based on Mishchenko et al. (2002). We calculate required

optical properties (mass extinction coefficients, extinction cross sections, single-scatter albedo, phase function expansion coef-
85   ficients) for each of the 11 mixtures at two wavelengths at both ends of the considered spectral range, and, if that mixture has
humidity-dependence, for 12 different relative humidity values.

Then, vertically resolved aerosol (dry) mass mixing ratio profiles for distinct aerosol mixtures, as provided by CAMS, are
sampled at the specific locations and times for each scene. For each vertical layer l, the extinction optical depth $\tau_{a,l}$ for an
aerosol mixture a is given by

$$\tau_{a,l} = \alpha_{a,l,\rho} \cdot \text{MMR}_{a,l} \cdot \frac{\Delta p_l}{g_l}, \tag{1}$$

where $\alpha_{a,l}, \rho$ is the aerosol mass extinction coefficient for mixture a ([m^2 kg^{-1}]) at specific humidity ρ, MMR_a is the mass
mixing ratio ([kg kg^{-1}]) for mixture a, and finally Δp_l is the pressure interval ([Pa]) for the given pressure layer l and g_l is the
acceleration of gravity ([m s^{-2}]) at the center of the pressure interval. This extinction optical depth is calculated for each layer
in the model atmosphere at the wavelengths at the edges of the wavelength window. Extinction and scattering profiles for each
95   wavelength in between those edges are then interpolated through an Ångstrom exponent ansatz.

The radiative transfer scheme (Heidinger et al., 2006; O'Dell et al., 2006; Natraj and Spurr, 2007; O'Dell, 2010) finally
ingests the total scene information, including the scattering properties for each mixture, to produce top-of-the-atmosphere
(TOA) radiances, which are then fed into the instrument model which then results in a synthetic measurement. We do not apply
instrument noise to the synthetic TOA radiances since we are interested in systematic errors. In the generation of the synthetic
100 TOA radiances, we ultimately use high-accuracy calculations corresponding to 24 streams.

A pivotal aspect of our aerosol scheme is the complexity of the ingested aerosol information. Assuming there are contribu-
tions from all five hygroscopic (with 12 different humidity values) and all six non-hygroscopic aerosol mixtures, there is a total
of 66 different aerosol components. The geographic distribution of total-column aerosol extinction is shown in Fig. 3.

We ingest the full aerosol profiles as prescribed by CAMS, rather than representing the vertical distribution as a simpler,
105 parameterized shape, which is done in various retrieval algorithms (O'Dell et al., 2018; Lorente et al., 2021). Some examples
of the vertical distribution of the aerosol mixtures is shown in Fig. 4.

The radiative transfer portion of the simulator can be run in a so-called "clear-sky" mode, in which absorption and scattering
due to clouds and aerosols is ignored, resulting in a Rayleigh-only atmosphere. While scattering due to the Rayleigh effect
could not be turned off, the very low amount of extinction due to Rayleigh scattering at 2.3 μm makes this effectively an
110 absorption-only set-up. This mode allows us to produce two sets synthetic top-of-the-atmosphere measurements, one in which
clouds and aerosols are present, and one without. Every other scene quantity is treated the same.

3   Retrieval algorithm set-up

We use a single-band algorithm which has been developed for the GeoCarb mission and was demonstrated in an earlier study
(Somkuti et al., 2021). The main retrieval window stretches from 2.324 μm to 2.338 μm, which contains absorption lines from

Atmospheric
Measurement
Techniques
Discussions
Open Access
EGU

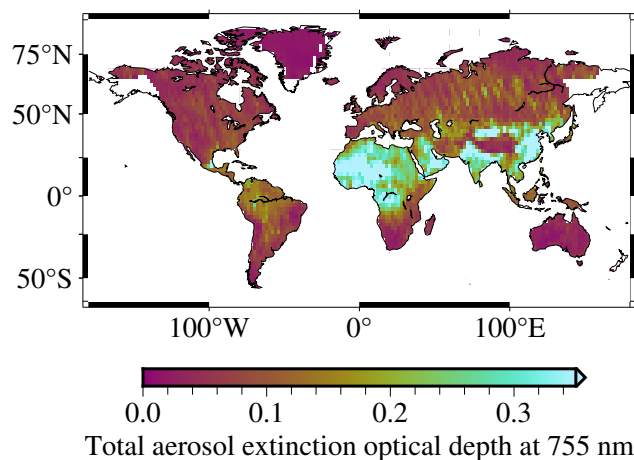**Figure 3.** A map showing the geographical distribution of total-column aerosol extinction optical depth, gridded to $2° \times 2°$ grid cells.
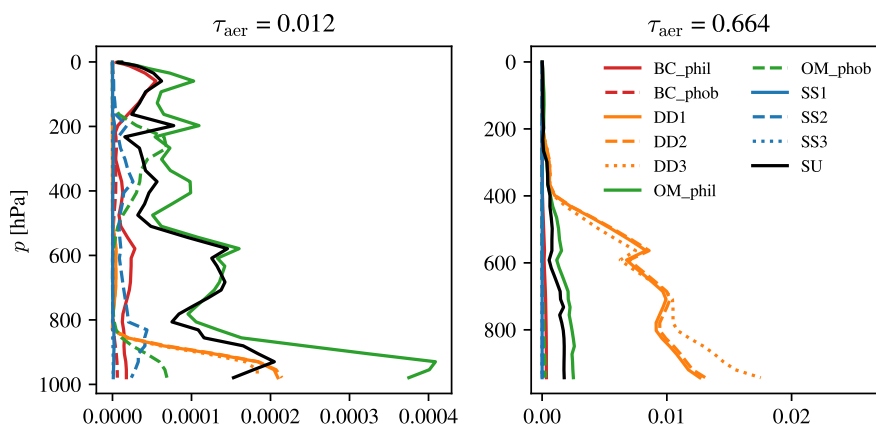

Figure 4. Two examples of the CAMS-derived aerosol profiles used in the generation of synthetic radiances. For this figure we aggregated all species into their respective type and size bins, regardless of their specific value of relative humidity. The example on the left shows a scene with low aerosol loading with contributions mostly from sulfates (SU) and hydrophilic organic matter (OM_phil). The example on the right, however, is dominated by all three size-bins of mineral dust (DD1, DD2, DD3). Hydrophobic organic matter (OM_phob), sea salt (SS1, SS2, SS3) and both types of black carbon (BC_phob, BC_phil) do not contribute significantly in these two examples. Note the complex shape of the vertical distributions in the left example, which would be very difficult to capture via a parametric description.

115 CH_4, CO and H_2O. This retrieval window is similar to what Schneising et al. (2019) have used, and does not cover the entire available range of the spectrometer. An example is shown in Fig. 5.

The forward model of the retrieval algorithm is conceptually equal to that of the simulator. Each scene is comprised of a layered atmosphere in which each layer is considered horizontally homogeneous in terms of their physical properties. At the layer boundaries, we set gas mixing ratios, pressure, temperature, and specific humidity. Optical properties of gases (CH_4,
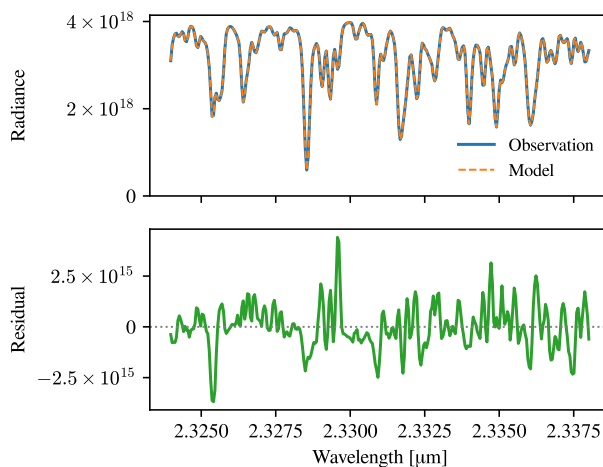
Atmospheric
Measurement
Techniques
Discussions

Open Access

EGU

Figure 5. Illustrative example of the used retrieval window between 2.324 μm and 2.338 μm. The top panel shows both the synthetic TOA spectrum ("observation") along with the fitted spectrum produced by the retrieval algorithm ("model"), and the spectral residual is shown in the bottom panel. Both are in units of [ph s^{-1} m^{-2} sr^{-1} μm^{-1}]. This particular example has a relative residual RMS of 0.03%.

120   CO and H$_2$O) are calculated via pre-calculated spectroscopy tables derived from HITRAN2016 (Gordon et al., 2017) that are sampled accordingly in the wavelength, temperature, pressure and humidity dimensions. More details on the calculation of those quantities can be found e.g. Cogan et al. (2012); Wu et al. (2018); OCO-2 Science Team (2019).

In our retrieval algorithm, we can switch freely between two major modes to perform the radiative transfer calculations. The first one employs the non-scattering Beer-Lambert-Bouguer law, in which we only account for extinction from gases and 125   Rayleigh scattering in an absorption-only atmosphere. The second mode invokes the XRTM radiative transfer library (McGarragh, 2020), which itself allows us to effortlessly switch between various numerical solvers, including different multiple-scattering ones. We use both radiative transfer modes as a means of understanding the robustness of our experiment.

Within the forward model of the retrieval algorithm, we are generally free to choose an arbitrary vertical layering scheme, however for this exercise, we choose the same exact pressure layers (and layer boundaries) as the simulator forward model, 40 130   layers in total, in order to minimize the impact of simulation-retrieval mismatch. Additionally, we can ingest the same compound aerosol information as is used in the simulator forward model to obtain the same aerosol profiles and the corresponding scattering properties.

The inverse method is based on Rodgers (2000) and is an iterative Bayesian scheme that maximizes the *a posteriori* probability density function. Given an iteration i, the state vector for the next iteration $i+1$ is calculated as

135
$$\mathbf{x}_{i+1} = \mathbf{x}_\mathrm{a} + \left(\mathbf{S}_\mathrm{a}^{-1} + \mathbf{K}^\mathrm{T}\mathbf{S}_\varepsilon^{-1}\mathbf{K}\right)^{-1}\mathbf{K}^\mathrm{T}\mathbf{S}_\varepsilon^{-1} \times$$
$$[\mathbf{y} - \mathbf{F}(\mathbf{x}_i) + \mathbf{K}(\mathbf{x}_i - \mathbf{x}_\mathrm{a})], \tag{2}$$

where $\mathbf{x}_\mathrm{a}$ is the *a priori* state vector, $\mathbf{S}_\mathrm{a}$ is the associated *a priori* covariance matrix, $\mathbf{S}_\varepsilon$ is the diagonal instrument noise covariance matrix, and $\mathbf{K}$ is the forward model Jacobian matrix evaluated at iteration i. We mentioned earlier (Section 2) that

the synthetic observations do not contain instrument noise, however we do use the GeoCarb noise model (Somkuti et al., 2021) for the calculation of a realistic $\mathbf{S}_\varepsilon$.

140   Our state vector contains the following elements: two polynomial coefficients to represent the spectrally varying surface albedo, two polynomial coefficients to represent the assignment between spectral sample and wavelength (also referred to as dispersion), one scale factor for each of the considered trace gas profiles of CH_4, CO and, H_2O, a temperature offset common to all vertical levels, and finally one value to adjust the spectral shift of the solar spectrum only. Values for the prior state vector $\mathbf{x}_a$ are obtained as follows: gas scale factors are set to 1.0, instrument dispersion coefficients are taken straight from the

145 instrument model, the solar shift is set to $0.0\,\mu m$, and the prior (and first guess) surface albedo is estimated from the radiances themselves via

$$\rho_0 = \frac{\pi \cdot \max(I)}{\max(L_0) \cdot \cos\theta_0}, \tag{3}$$

where I is the measured TOA radiance, L_0 is the solar irradiance for the same retrieval window, and θ_0 is the solar zenith angle. The prior value for the albedo slope coefficient (ρ_1) is $0.0\,\mu m^{-1}$ for every scene. We make the choice to set the zeroth

150 iteration to be equal to the prior state vector ($\mathbf{x}_0 = \mathbf{x}_a$). As this is a so-called "scaling retrieval" in which the trace gas profiles are not changed within the iterative scheme, we must pick a profile shape to be scaled by the retrieval algorithm. We choose to use the true shape as they are used in the simulation forward model.

    Iterations are halted as soon as one of these three criteria are met: the number of allowed iterations is reached, the change in reduced chi-squared statistic (modeled versus observed radiance) is smaller than 1%, the value in $d\sigma^2$ is less than the number

155 of state vector elements, where

$$d\sigma^2 = (\mathbf{x}_{i+1} - \mathbf{x}_i)\hat{\mathbf{S}}^{-1}(\mathbf{x}_{i+1} - \mathbf{x}_i), \tag{4}$$

with $\hat{\mathbf{S}}$ being the *a posteriori* covariance matrix defined as

$$\hat{\mathbf{S}} = \left(\mathbf{S}_a^{-1} + \mathbf{K}^T\mathbf{S}_\varepsilon\mathbf{K}\right)^{-1}. \tag{5}$$

4   Results and analysis

160 The simulation experiments and subsequent analyses are organized in the following manner. First, we present a baseline scenario in which aerosols were ignored during the RT simulations and the retrieval forward model. Already in this baseline scenario we see a surface-dependent XCH_4 bias appearing. This is a key finding, as it establishes the fact that an interplay between apparent surface reflectance and retrieved XCH_4 is already present in an absorption-only atmosphere as a consequence of the retrieval forward model error. Then, we introduce aerosols into the RT simulations, and keep everything else exactly the

165 same, i.e. not accounting for aerosols in the retrieval. This is where we observe a strong enhancement of the surface bias. Finally, we add the aerosol truth to the retrieval algorithm and observe a significant mitigation of the enhanced surface bias.

    For the first two scenarios we use two different RT schemes - a non-scattering one, and a single-scatter model from the dedicated XRTM code. The non-scattering RT scheme is referred to as "non-sc" in various figures, and the single-scatter one

is labeled as "SS". In a model atmosphere without scattering, the two approaches should yield the same result. However due to

170   the numerical nature of RT codes, and the whole algorithm itself, small differences are to be expected and we utilize the two

RT models as a form of validation. Ideally, we should observe biases and regional patterns thereof in the same places with both

non-scattering and single-scattering models.

The experiments are laid out in a flowchart in Fig. 6 to allow the reader quick inspection of the relationship between simulator

forward model set-up, and the corresponding retrieval algorithm set-up.

175   4.1   Baseline, clear-sky case

We first analyze the retrieval results based on simulations in which scattering from aerosols and clouds was ignored. This

clear-sky case is considered the baseline scenario, labeled (CS1) and (CS2) in the flowchart shown in Fig. 6.

Here we like to remind the reader again that the forward model of the retrieval algorithm and the forward model of the sim-

ulator (which generates the synthetic measurements) are different. Since we force several aspects of the simulator and retrieval

180   forward models to be the same, such as vertical layering, meteorological inputs, trace gas profile shapes and spectroscopy

tables, this constitutes a *best-case* scenario. However we must emphasize that while many of the key ingredients in the simu-

lator and retrieval forward models are the same, they do not produce numerically the same TOA radiances for the same set of

atmospheric and surface properties. Thus, even for a clear-sky set-up for both simulator and retrieval forward model, there are

forward model errors which cause retrieval errors.

185   Scenes from the clear-sky case are then run through the retrieval algorithm twice, with two different approaches for the

radiative transfer calculations: once with the non-scattering model (non-sc), and once with the single-scattering model (SS).

While there are almost no contributions from scattering in this set of synthetic measurements (Rayleigh scattering is present,

but negligible), we chose to perform retrievals with the two mentioned RT schemes to provide robustness to the results.

For selecting the final subset of scenes to be analyzed, we apply very basic quality filtering criteria to remove retrievals that

190   either did not converge within the maximally allowed number of iterations $N_{\mathrm{itermax}} = 3$, have a solar zenith angle θ_0 above

the threshold of $75°$ or have a spectral residual reduced χ^2 larger than 0.1. Note that the χ^2 values here are low due to the fact

that we did not add instrument noise to the synthetic measurements, however we still use χ^2 as a measure of fit quality.

As for bias correction, we only remove a single offset term which is the median of the ensemble difference between retrieved

and true XCH_4. This correction brings the overall bias, per design, to 0.0 ppb, such that the error maps highlight regional-scale

195   differences.

The maps in Fig. 7 show the XCH_4 errors for the two sets of retrievals (non-scattering, single scattering). Errors, meaning

the difference between retrieved (and bias-corrected) and the truth, were calculated using the retrieval averaging kernels for

each individual scene, as well as accounting for the prior methane profiles according to Wunch et al. (2011). Each set exhibits

a small overall offset between -6 ppb and -3 ppb, and small overall scatter ≤ 2 ppb. Errors show a geographic pattern with

200   error enhancements in the tropics, and we find these errors be statistically significant, but weak linear functions of surface
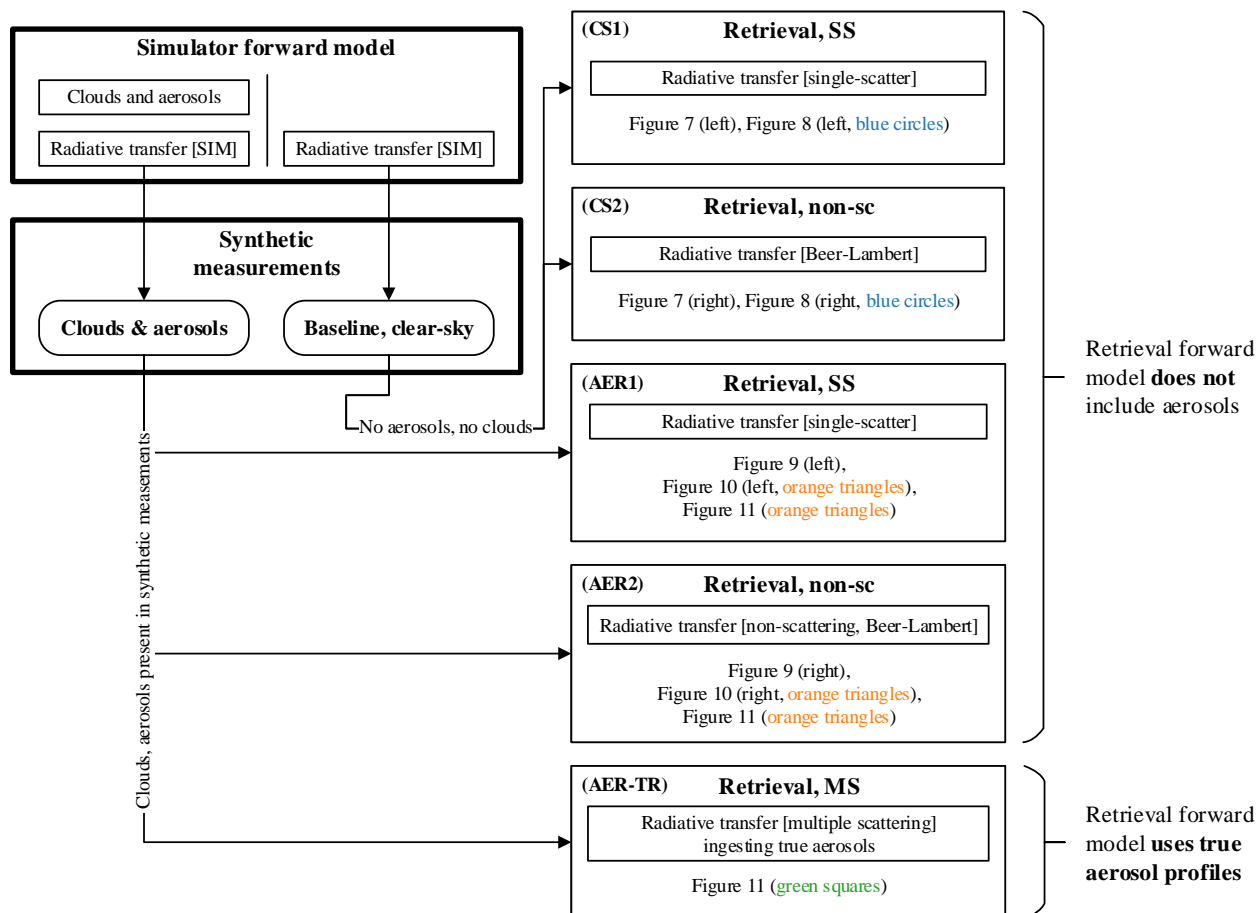
reflectance and solar angles.

Figure 6. A flowchart illustrating the retrieval experiment set-ups. We generate two sets of synthetic measurements with the simulator forward model: one accounting for clouds and aerosols (left path) and one where clouds and aerosols are ignored (right path, clear-sky). The first two experiments enter both Fig. 7 and Fig. 9, labeled as (CS1) and (CS2): they represent the clear-sky retrievals from clear-sky simulations using two different RT model codes on the retrieval side. In bias plots (e.g. Fig. 9), they correspond to the blue circles. The second set of retrieval experiments, (AER1) and (AER2), follow the left path, where clouds and aerosols were present in the simulator forward model RT, however the retrieval RT still does not include aerosols. The results from (AER1) and (AER2) are shown in Fig. 8, Fig. 9 and Fig. 10, and they are always shown as orange triangles in the bias plots. Finally, the retrieval experiment denoted as (AER-TR) is based on the same synthetic measurements as (AER1) and (AER2), however the retrieval forward model now includes the true aerosol profiles, along with an appropriate multiple-scattering RT solver. In the final bias plot, Fig. 11, these results are shown as green squares.

The spatial distribution of errors shown in Fig. 7 provide some geographical context to the biases mentioned above. We see a contrast between areas with predominantly dark surfaces at 2.3 μm, such as the central African and South American tropical rainforests, and regions with much higher surface reflectance, such as the deserts. Note, however, that the overall magnitude
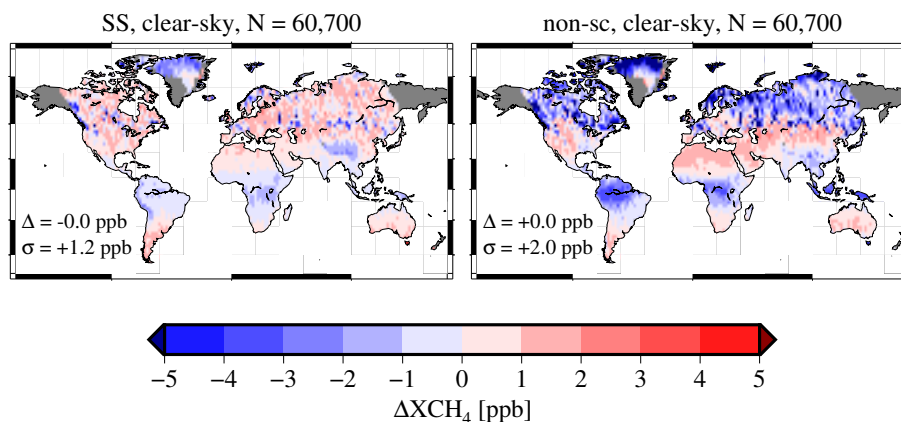
Figure 7. Maps of mean-removed retrieval errors for the clear-sky scenario in which no aerosols nor clouds were used during the forward radiative transfer simulations. Single-scattering radiative transfer on the left, absorption-only radiative transfer on the right - experiments (CS1) and (CS2), respectively (Fig. 6). The strongest regional highlights are seen in tropical forests where the surface reflectance at 2.4 µm is low. The total number of scenes for a given map is shown, since each set is quality-filtered separately, which can lead to a slightly different number of retrievals plotted.

of these systematic errors is small. Noise driven errors for the GeoCarb instrument, for example, would be expected to be one order of magnitude larger.

4.2 Inclusion of aerosols in the simulations

Building on the results presented in Section 4.1, we now introduce a single change. In the forward RT simulations, which produce the synthetic measured radiances, we switch on aerosols and clouds, however leave the retrieval set-up the same. In the flowchart (Fig. 6), these experiments are labeled as (AER1) and (AER2). The retrieval algorithms are ignorant to the fact that the synthetic measurements now reflect a more realistic atmosphere in which multiple scattering via tropospheric aerosols has taken place. To remind readers, while the full produced data set includes scenes with thick water and ice clouds, we omit those scenes for this study.

We repeat the procedure from above and subtract the overall median error before producing the maps in Fig. 8. When compared to Fig. 7 (note the differently scaled colorbars), we observe a much stronger contrast between central tropical Africa and the surrounding regions with brighter surfaces, and similarly see such a contrast between the scenes over the Tibetan plateau and surrounding areas. More importantly, the magnitude of the bias increased by a factor of roughly 4.

The change in the retrieved XCH_4 is purely driven by introducing aerosols into the forward model. We can represent this surface reflectance bias by grouping scenes into discrete bins of retrieved (or apparent) surface albedo and then calculating, for each scene, the ratio of true to retrieved XCH_4. This is shown in Fig. 9. For darker surfaces with apparent albedo less than 0.2, there is a clear low-bias, whereas a high-bias is observed for brighter surfaces with apparent albedo larger than 0.5. This
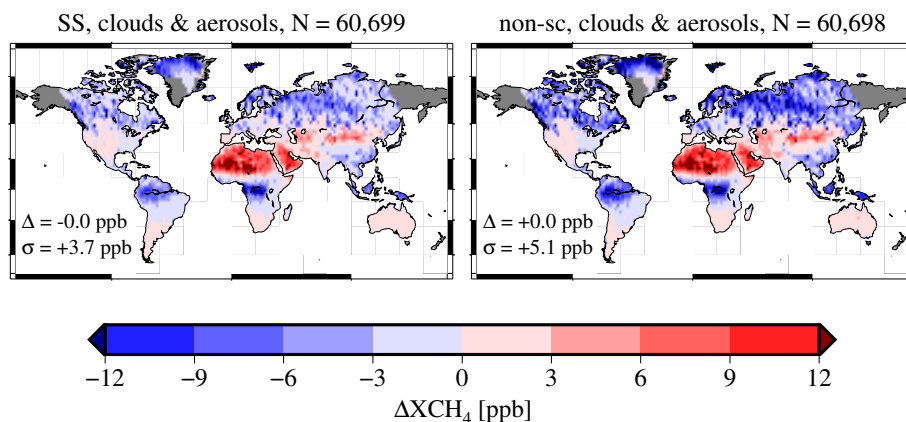
Figure 8. Error maps, similar to Fig. 7, however for model atmospheres in which aerosols and clouds are present. The regional contrasts between densely vegetated areas with low surface reflectance (tropical rainforests) and their surrounding areas (e.g. the Sahara desert) appear brighter in the 2.3 μm wavelength range. These are the results of expriments (AER1) and (AER2) when comparing to the flowchart in Fig. 6.
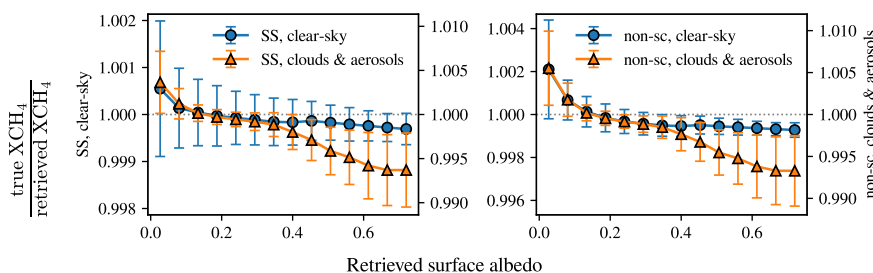

Figure 9. Curves that show surface reflectance bias: the ratio of true and retrieved XCH_4 as a function of the apparent surface albedo. For this figure, we first assign each retrieval scene to a bin according to the retrieved surface albedo. The circles (clear-sky) and triangles (with aerosols) then represent the median of all values within the bin, and the error bars are the robust standard deviation of the bin, calculated as the inter-quartile range divided by 1.349. This statistic is used for all other error bars in this manuscript. Note that the clear-sky observations (circles, left y-axis) and the ones with aerosols (triangles, right y-axis) are plotted on separate ordinates to make a qualitative comparison of the shape easier. The scale of the bias in the "cloudy & aerosols" scenario is roughly an order of magnitude larger. Blue circles represent the results of experiments (CS1) and (CS2), orange triangles represent the results of (AER1) and (AER2) when comparing to the flowchart in Fig. 6.

observed bias is quantitatively comparable to that seen in TROPOMI-derived XCH_4, as first introduced in Lorente et al. (2021) and further elaborated in Lorente et al. (2023).

225   We make the following important observations. The surface reflectance bias already appears in clear-sky simulations and shows the underestimation of XCH_4 for dark surfaces in a very similar qualitative manner. Once the apparent surface albedo is larger than roughly 0.3, however, there is no significant bias seen for clear-sky scenes. The retrievals from the aerosol-laden
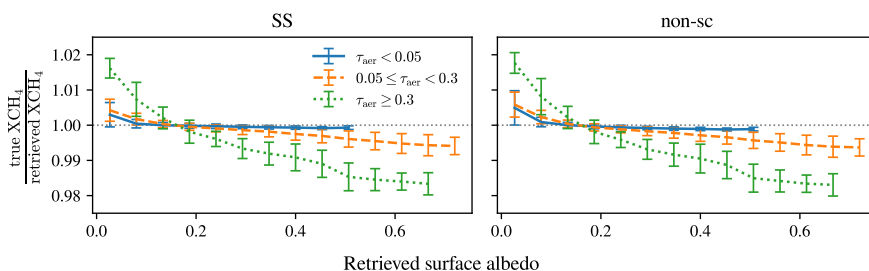
Figure 10. Bias curves, similar to Fig. 9, but without clear-sky simulations. On the left, the results of experiment (AER1) aer shown, whereas the right panel are the results of expriment (AER2). The two retrieval sets, with either the single-scattering (SS) or the non-scattering (non-sc) RT model, are split into sub-sets of different regimes of total aerosol extinction optical depth τ_{aer} (at a reference wavelength of 755 nm). This figure shows that the underestimation of XCH_4 for dark surfaces with albedo less than 0.1 is mainly driven by scenes with larger aerosol loadings.

scenes, however, show further dependence on the apparent surface albedo. Such a bias would imprint surface features on e.g. desert scenes like those shown in Fig. 1.

We note that the surface reflectance bias discussed in Lorente et al. (2021, 2023) is larger in magnitude, but shows the same
230 general shape as our result in qualitative terms. The observed surface reflectance bias as shown in Fig. 9 is the result of a global aggregate. When the same figure is produced for various subsets, separately, however, we see that the strength of the bias changes as a result of the amount of aerosols within that subset. In Fig. 10, we group the global set of scenes into two subsets of different total aerosol extinction optical depths τ_{aer}. Through this figure, we can observe that the underestimation of XCH_4 for darker surfaces gets larger with increasing aerosol loadings. Notice the kink near albedo value of ≈ 0.4 in Fig. 9
235 that is seen for the simulation set that includes clouds and aerosols (orange, triangles), which is absent in any of the curves in Fig. 10. Since the total aerosol extinction per scene is not equally distributed amongst the bins of apparent surface reflectance, we suspect the observed kink in the bias curve to be a result of a sampling bias which blends together the various curves of different τ_{aer} regimes. This is investigated in Fig. 10 in which we produce bias curves for different bins of aerosol loadings.

We do not find any significant impact of the aerosol single scattering albedo on the bias, suggesting that the total aerosol
240 extinction is the main driver in the case of single-band retrievals of this type.

4.3 Mitigation by accounting for true aerosol profiles in the retrieval

In Sections 4.1 and 4.2 we have observed that the surface reflectance bias is already present in clear-sky conditions, but is strongly enhanced when aerosols are introduced in the RT simulations that produce the synthetic measurements. Consistent with that notion is the fact the dependency of the error grows with larger aerosol abundances, as shown in Fig 10.
245 An obvious way to mitigate the surface reflectance bias is to inform the retrieval algorithm about the aerosol scattering profile that is present in the scene. We implement this straightforwardly by adding the layer-resolved aerosol extinction and scattering
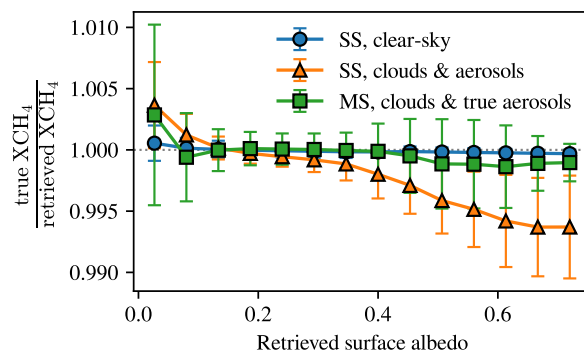
Atmospheric
Measurement
Techniques
Discussions

Figure 11. Surface reflectance bias similar to Fig. 9. In this figure, however, the third curve (squares, green), is derived from retrievals for which the true aerosol profiles were ingested as part of the retrieval algorithm forward model. This is expriment (AER-TR) in the flowchart (Fig. 6). We observe that, when comparing to the unmitigated runs (triangles, orange) of experiment (AER1) no significant bias remains. This suggests that better constraining aerosols is key to mitigating these types of retrieval biases.

optical depths to the (forward) model used during the retrieval, appropriately adding the phase function expansion coefficients with their correct relative weights to obtain a match of the total optical properties used by the simulator (see Sec. 2). Then, we also switch the RT model in the retrieval algorithm to use multiple scattering via a discrete ordinate solver with 16 streams (8 per hemisphere). This is necessary since using a single-scattering RT model, while also incorporating the true aerosol profiles in the retrieval forward model, does not result in a mitigation of the observed bias. In the flowchart (Fig. 6), this set-up is labeled as experiment (AER-TR).

The result is shown in Fig. 11, in which we overlay the described approach with an earlier result that used a single-scattering RT model without any knowledge of the aerosol profiles. For nadir viewing geometry, the bias curve exhibits much smaller dependency on the surface albedo when compared to the original approach. This result shows that the mitigation strategy is successful in reducing the surface bias and almost brings it to the same level as observed for the clear-sky scenario.

5 Discussion & Conclusions

In this study, we analyzed the impact of tropospheric aerosols on biases of XCH_4 obtained from single-band retrievals from the 2.3 μm absorption window. We were able to demonstrate that a weak surface-dependent bias is present already in clear-sky conditions, however aerosols can amplify those retrieval biases, and the effect grows with aerosol abundance as shown in Fig. 9.

The significance of our result is related to actual findings from the TROPOMI instrument, which have been discussed by Lorente et al. (2021, 2023). Surface reflectance biases in retrieved XCH_4 are a troublesome feature, since surface patterns on the ground will manifest as gradients of total column methane which can lead to wrong estimates of e.g. emission rates or the emergence of artificial features (Froitzheim et al., 2021; Schneising et al., 2023). In the past, studies have required an ad-hoc

265 correction to remove the surface reflectance bias in the XCH_4 fields (Liu et al., 2021) or remove scenes entirely which show a large correlation between XCH_4 and surface albedo (Sadavarte et al., 2021).

While the bias that we observe in our study is qualitatively similar to that seen in Lorente et al. (2021, 2023), we want to highlight that there are several differences in our instrument model and that of the TROPOMI instrument, as well as some key differences in our retrieval approach. First, the spectral resolution of the TROPOMI spectrometer for the SWIR band is

270 ≈ 0.25 nm, where as our instrument model, derived for the GeoCarb instrument, is closer to ≈ 0.12 nm. Further, we utilize a single-band retrieval, whereas Lorente et al. (2021, 2023) co-retrieve the oxygen A-band at 0.76 µm, which, in general, should allow for better constraining of the retrieved aerosol abundance. Lastly, in our simulations (Section 2), we do not introduce any instrument or calibration artefacts such as, but not limited to, remaining stray light, imperfect radiometric calibration or imperfect knowledge of detector (non-)linearity. This, in turn, also supports the argument that the biases observed in TROPOMI

275 data are not caused by any instrument-related issues or calibration deficiencies, but are intrinsic to the retrieval approach from the 2.3 µm band.

In Section 4.3, we demonstrate the impact of perfect knowledge of the tropospheric aerosol profiles. Once the retrieval algorithm is aided by inserting the true aerosol distributions into each scene, most of the surface reflectance bias is mitigated, as shown in Fig. 11, where we obtain results that are similar to those for the clear-sky scenario. This result shows the importance

280 of better constraining the overall aerosol information for use in retrieval algorithms, as has been previously stated in different contexts (Bell et al., 2023; Rusli et al., 2021). Aerosol-driven biases are of such concern, that for the upcoming Copernicus CO2M mission, developed by the European Space Agency to monitor anthropogenic carbon dioxide emissions, a dedicated aerosol instrument will be part of the payload in order to improve the quality of the XCO_2 retrievals (Sierk et al., 2021). While our study does not allow for any conclusions to be drawn for the CO2M mission regarding possible surface biases and their

285 enhancement due to aerosols, the specific instrument could be investigated using our observing system simulation experiment set-up.

We have shown that incorporating the true aerosol information mostly removes the surface reflectance bias for nadir-viewing observations, however implementing this approach in a real science data processing scenario might not be feasible. It needs to be shown yet if globally covering aerosol forecasts, e.g. CAMS (Copernicus) or GEOS-5 (Molod et al., 2015), are close enough

290 to the truth to be treated as such in the retrieval forward model for the purpose of mitigating the discussed bias. In general, limitations on data processing resources might ultimately necessitate the usage of faster forward models that could introduce biases similar as shown here. We have observed that the bias seems to be driven by the total aerosol extinction optical depths in the scene, rather than the vertical distribution or how absorbing the aerosols are. A future study could examine whether the a simpler aerosol profile than those shown in Fig. 4, while conserving the total aerosol extinction optical depth, would be just

295 as effective in mitigating the surface reflectance bias.

Another important aspect of our study is the chosen absorption window. We investigated the 2.3 µm window as both the TROPOMI and the GeoCarb instruments are equipped with corresponding spectrometers. However, there is no reason to assume that the same behavior arises with retrievals from the 1.65 µm window, as featured on e.g. GOSAT (Kuze et al., 2009)

Atmospheric
Measurement
Techniques
Discussions

Open Access

EGU

or MethaneSAT (Chan Miller et al., 2023). In fact, Chan Miller et al. (2023) present first results from the airborne MethaneAir
300   instrument and do not observe any strong surface-related biases.

In our analysis we found scenes measured in sunglint-following viewing geometry to behave distinctly different from nadir-viewing ones. The surface bias shows a qualitatively different shape and the mitigation effort through implementing aerosol truth information did not work as well as with nadir-viewing scenes. Efforts to understand the cause of this discrepancy did not yield any satisfying answers. Given the small absolute magnitude of the effect, however, we hypothesize that some
305   inconsistency in the set-up of the retrieval RT and the simulation RT codes is the main cause.

Finally, we want to again highlight the results of the clear-sky baseline scenario presented in Section 4.1. Even in almost ideal circumstances where meteorology, spectroscopy and trace gas profiles are known perfectly, an optimal-estimation based retrieval exhibits a small but significant surface-dependent XCH_4 bias. We suspect that this is an inherent consequence of the 2.3 μm band, which does not have a clear continuum portion via which surface reflectance and methane abundance can
310   be sufficiently disentangled. Thus, a mission designed for the remote sensing of methane from the 2.3 μm absorption band will likely require a surface bias correction procedure as a core part of its operations concept. As long as the surface bias is sufficiently characterized, an appropriate correction can effectively mitigate the impact on the retrieved XCH_4 field.

Code and data availability. The results of the study, i.e. the results of retrievals and the truth values, as well as a Python notebook that produces the figures used in this manuscript, can be downloaded from Zenodo at https://zenodo.org/records/13285730 (DOI:10.5281/zenodo.13285730).

Atmospheric
Measurement
Techniques
Discussions

References

Bell, E., O'Dell, C. W., Taylor, T. E., Merrelli, A., Nelson, R. R., Kiel, M., Eldering, A., Rosenberg, R., and Fisher, B.: Exploring bias in the OCO-3 snapshot area mapping mode via geometry, surface, and aerosol effects, Atmospheric Measurement Techniques, 16, 109–133, https://doi.org/10.5194/amt-16-109-2023, 2023.

Bozzo, A., Benedetti, A., Flemming, J., Kipling, Z., and Rémy, S.: An aerosol climatology for global models based on the tropospheric aerosol scheme in the Integrated Forecasting System of ECMWF, Geoscientific Model Development, 13, 1007–1034, https://doi.org/10.5194/gmd-13-1007-2020, 2020.

Chan Miller, C., Roche, S., Wilzewski, J. S., Liu, X., Chance, K., Souri, A. H., Conway, E., Luo, B., Samra, J., Hawthorne, J., Sun, K., Staebell, C., Chulakadabba, A., Sargent, M., Benmergui, J. S., Franklin, J. E., Daube, B. C., Li, Y., Laughner, J. L., Baier, B. C., Gautam, R., Omara, M., and Wofsy, S. C.: Methane retrieval from MethaneAIR using the CO_2 Proxy Approach: A demonstration for the upcoming MethaneSAT mission, EGUsphere, 2023, 1–40, https://doi.org/10.5194/egusphere-2023-1962, 2023.

Cogan, A. J., Boesch, H., Parker, R. J., Feng, L., Palmer, P. I., Blavier, J.-F., Deutscher, N. M., MacAtangay, R., Notholt, J., Roehl, C., Warneke, T., and Wunch, D.: Atmospheric carbon dioxide retrieved from the Greenhouse gases Observing SATellite (GOSAT): Comparison with ground-based TCCON observations and GEOS-Chem model calculations, Journal of Geophysical Research Atmospheres, 117, https://doi.org/10.1029/2012JD018087, 2012.

Copernicus: Copernicus homepage, https://atmosphere.copernicus.eu/, accessed: April 11, 2023.

Copernicus Sentinel-5P: TROPOMI Level 2 Methane Total Column products (processed by ESA), Tech. Rep. Version 02, European Space Agency, https://doi.org/10.5270/S5P-3lcdqiv, 2021.

Crisp, D.: Measuring atmospheric carbon dioxide from space with the Orbiting Carbon Observatory-2 (OCO-2), in: Earth Observing Systems XX, edited by Butler, J. J., Xiong, X. J., and Gu, X., vol. 9607, pp. 1 – 7, International Society for Optics and Photonics, SPIE, https://doi.org/10.1117/12.2187291, 2015.

Crisp, D., Atlas, R., Breon, F.-M., Brown, L., Burrows, J., Ciais, P., Connor, B., Doney, S., Fung, I., Jacob, D., Miller, C., O'Brien, D., Pawson, S., Randerson, J., Rayner, P., Salawitch, R., Sander, S., Sen, B., Stephens, G., Tans, P., Toon, G., Wennberg, P., Wofsy, S., Yung, Y., Kuang, Z., Chudasama, B., Sprague, G., Weiss, B., Pollock, R., Kenyon, D., and Schroll, S.: The Orbiting Carbon Observatory (OCO) mission, Advances in Space Research, 34, 700–709, https://doi.org/10.1016/j.asr.2003.08.062, trace Constituents in the Troposphere and Lower Stratosphere, 2004.

Eldering, A., Taylor, T. E., O'Dell, C. W., and Pavlick, R.: The OCO-3 mission: measurement objectives and expected performance based on 1 year of simulated data, Atmospheric Measurement Techniques, 12, 2341–2370, https://doi.org/10.5194/amt-12-2341-2019, 2019.

Frankenberg, C., O'Dell, C., Berry, J., Guanter, L., Joiner, J., Köhler, P., Pollock, R., and Taylor, T. E.: Prospects for chlorophyll fluorescence remote sensing from the Orbiting Carbon Observatory-2, Remote Sensing of Environment, 147, 1–12, https://doi.org/10.1016/j.rse.2014.02.007, 2014.

Froitzheim, N., Majka, J., and Zastrozhnov, D.: Methane release from carbonate rock formations in the Siberian permafrost area during and after the 2020 heat wave, Proceedings of the National Academy of Sciences, 118, e2107632 118, https://doi.org/10.1073/pnas.2107632118, 2021.

Gordon, I. E., Rothman, L. S., Hill, C., Kochanov, R. V., Tan, Y., Bernath, P. F., Birk, M., Boudon, V., Campargue, A., Chance, K., et al.: The HITRAN2016 molecular spectroscopic database, Journal of Quantitative Spectroscopy and Radiative Transfer, 203, 3–69, 2017.

Atmospheric
Measurement
Techniques
Discussions

Harris, C. R., Millman, K. J., van der Walt, S. J., Gommers, R., Virtanen, P., Cournapeau, D., Wieser, E., Taylor, J., Berg, S., Smith, N. J., et al.: Array programming with NumPy, Nature, 585, 357–362, https://doi.org/10.1038/s41586-020-2649-2, 2020.

365 Hasekamp, O., Lorente, A., Hu, H., Butz, A., aan de Brugh, J., and Landgraf, J.: Algorithm Theoretical Baseline Document for Sentinel-5 Precursor Methane Retrieval, 2019.

Heidinger, A. K., O'Dell, C., Bennartz, R., and Greenwald, T.: The successive-order-of-interaction radiative transfer model. Part I: Model development, Journal of applied meteorology and climatology, 45, 1388–1402, https://doi.org/10.1175/JAM2387.1, 2006.

Hunter, J. D.: Matplotlib: A 2D graphics environment, Computing in science & engineering, 9, 90–95, 370 https://doi.org/10.1109/MCSE.2007.55, 2007.

Kluyver, T., Ragan-Kelley, B., Pérez, F., Granger, B., Bussonnier, M., Frederic, J., Kelley, K., Hamrick, J., Grout, J., Corlay, S., Ivanov, P., Avila, D., Abdalla, S., Willing, C., and development team, J.: Jupyter Notebooks - a publishing format for reproducible computational workflows, in: Positioning and Power in Academic Publishing: Players, Agents and Agendas, edited by Loizides, F. and Scmidt, B., pp. 87–90, IOS Press, Netherlands, https://doi.org/10.3233/978-1-61499-649-1-87, 2016.

375 Kuze, A., Suto, H., Nakajima, M., and Hamazaki, T.: Thermal and near infrared sensor for carbon observation Fourier-transform spectrometer on the Greenhouse Gases Observing Satellite for greenhouse gases monitoring, Applied optics, 48, 6716–6733, https://doi.org/10.1364/AO.48.006716, 2009.

Liu, M., van der A, R., van Weele, M., Eskes, H., Lu, X., Veefkind, P., de Laat, J., Kong, H., Wang, J., Sun, J., Ding, J., Zhao, Y., and Weng, H.: A New Divergence Method to Quantify Methane Emissions Using Observations of Sentinel-5P TROPOMI, Geophysical Research 380 Letters, 48, e2021GL094 151, https://doi.org/10.1029/2021GL094151, e2021GL094151 2021GL094151, 2021.

Lorente, A., Borsdorff, T., Butz, A., Hasekamp, O., aan de Brugh, J., Schneider, A., Wu, L., Hase, F., Kivi, R., Wunch, D., Pollard, D. F., Shiomi, K., Deutscher, N. M., Velazco, V. A., Roehl, C. M., Wennberg, P. O., Warneke, T., and Landgraf, J.: Methane retrieved from TROPOMI: improvement of the data product and validation of the first 2 years of measurements, Atmospheric Measurement Techniques, 14, 665–684, https://doi.org/10.5194/amt-14-665-2021, 2021.

385 Lorente, A., Borsdorff, T., Martinez-Velarte, M. C., and Landgraf, J.: Accounting for surface reflectance spectral features in TROPOMI methane retrievals, Atmospheric Measurement Techniques, 16, 1597–1608, https://doi.org/10.5194/amt-16-1597-2023, 2023.

McGarragh, G. R.: XRTM, https://github.com/gmcgarragh/xrtm, 2020.

McGarragh, G. R., O'Dell, C. W., Crowell, S. M. R., Somkuti, P., Burgh, E. B., and Moore III, B.: The GeoCarb greenhouse gas retrieval algorithm: simulations and sensitivity to sources of uncertainty, Atmospheric Measurement Techniques, 17, 1091–1121, 390 https://doi.org/10.5194/amt-17-1091-2024, 2024.

McKinney, W. et al.: pandas: a foundational Python library for data analysis and statistics, Python for High Performance and Scientific Computing, 14, 2011.

Mishchenko, M. I., Travis, L. D., and Lacis, A. A.: Scattering, absorption, and emission of light by small particles, Cambridge university press, 2002.

395 Molod, A., Takacs, L., Suarez, M., and Bacmeister, J.: Development of the GEOS-5 atmospheric general circulation model: Evolution from MERRA to MERRA2, Geoscientific Model Development, 8, 1339–1356, https://doi.org/10.5194/gmd-8-1339-2015, 2015.

Moore III, B., Crowell, S. M., Rayner, P. J., Kumer, J., O'Dell, C. W., O'Brien, D., Utembe, S., Polonsky, I., Schimel, D., and Lemen, J.: The potential of the geostationary Carbon Cycle Observatory (GeoCarb) to provide multi-scale constraints on the carbon cycle in the Americas, Frontiers in Environmental Science, 6, 109, https://doi.org/10.3389/fenvs.2018.00109, 2018.

400 Natraj, V. and Spurr, R. J.: A fast linearized pseudo-spherical two orders of scattering model to account for polarization in ver-
     tically inhomogeneous scattering–absorbing media, Journal of Quantitative Spectroscopy and Radiative Transfer, 107, 263–293,
     https://doi.org/10.1016/j.jqsrt.2007.02.011, 2007.

Nivitanont, J., Crowell, S. M., and Moore III, B.: A scanning strategy optimized for signal-to-noise ratio for the Geostationary Carbon Cycle
     Observatory (GeoCarb) instrument, Atmospheric Measurement Techniques, 12, 3317–3334, https://doi.org/10.5194/amt-12-3317-2019,
405 2019.

O'Brien, D. M., Polonsky, I., O'Dell, C., and Carheden, A.: Orbiting Carbon Observatory (OCO), algorithm theoretical basis document: The
     OCO simulator, Technical report ISSN 0737-5352-85, Cooperative Institute for Research in the Atmosphere, Colorado State University,
     2009.

OCO-2 Science Team: Orbiting Carbon Observatory (OCO) - 2 Level 2 Full Physics Algorithm Theoretical Basis Document, https://disc.
410 gsfc.nasa.gov/information/documents?title=OCO-2%20Documents, 2019.

O'Dell, C. W.: Acceleration of multiple-scattering, hyperspectral radiative transfer calculations via low-streams interpolation, Journal of
     Geophysical Research: Atmospheres, 115, https://doi.org/10.1029/2009JD012803, 2010.

O'Dell, C. W., Eldering, A., Wennberg, P. O., Crisp, D., Gunson, M. R., Fisher, B., Frankenberg, C., Kiel, M., Lindqvist, H., Mandrake, L.,
     Merrelli, A., Natraj, V., Nelson, R. R., Osterman, G. B., Payne, V. H., Taylor, T. E., Wunch, D., Drouin, B. J., Oyafuso, F., Chang, A.,
415 McDuffie, J., Smyth, M., Baker, D. F., Basu, S., Chevallier, F., Crowell, S. M. R., Feng, L., Palmer, P. I., Dubey, M., García, O. E., Griffith,
     D. W. T., Hase, F., Iraci, L. T., Kivi, R., Morino, I., Notholt, J., Ohyama, H., Petri, C., Roehl, C. M., Sha, M. K., Strong, K., Sussmann,
     R., Te, Y., Uchino, O., and Velazco, V. A.: Improved retrievals of carbon dioxide from Orbiting Carbon Observatory-2 with the version 8
     ACOS algorithm, Atmospheric Measurement Techniques, 11, 6539–6576, https://doi.org/10.5194/amt-11-6539-2018, 2018.

O'Dell, C. W., Heidinger, A. K., Greenwald, T., Bauer, P., and Bennartz, R.: The successive-order-of-interaction radiative trans-
420 fer model. Part II: Model performance and applications, Journal of applied meteorology and climatology, 45, 1403–1413,
     https://doi.org/10.1175/JAM2409.1, 2006.

Polonsky, I. N., O'Brien, D. M., Kumer, J. B., O'Dell, C. W., and the geoCARB Team: Performance of a geostationary mission,
     geoCARB, to measure CO_2, CH_4 and CO column-averaged concentrations, Atmospheric Measurement Techniques, 7, 959–981,
     https://doi.org/10.5194/amt-7-959-2014, 2014.

425 Rodgers, C. D.: Inverse methods for atmospheric sounding: theory and practice, vol. 2, World scientific, 2000.

Rusli, S. P., Hasekamp, O., aan de Brugh, J., Fu, G., Meijer, Y., and Landgraf, J.: Anthropogenic CO_2 monitoring satellite mission: the need
     for multi-angle polarimetric observations, Atmospheric Measurement Techniques, 14, 1167–1190, https://doi.org/10.5194/amt-14-1167-
     2021, 2021.

Sadavarte, P., Pandey, S., Maasakkers, J. D., Lorente, A., Borsdorff, T., Denier van der Gon, H., Houweling, S., and Aben, I.: Methane
430 Emissions from Superemitting Coal Mines in Australia Quantified Using TROPOMI Satellite Observations, Environmental Science &
     Technology, 55, 16 573–16 580, https://doi.org/10.1021/acs.est.1c03976, 2021.

Schaaf, C. and Wang, Z.: MCD43A1 MODIS/Terra+Aqua BRDF/Albedo Model Parameters Daily L3 Global - 500m V006,
     https://doi.org/10.5067/MODIS/MCD43A1.006, 2015.

Schneising, O., Buchwitz, M., Reuter, M., Bovensmann, H., Burrows, J. P., Borsdorff, T., Deutscher, N. M., Feist, D. G., Griffith, D. W., Hase,
435 F., et al.: A scientific algorithm to simultaneously retrieve carbon monoxide and methane from TROPOMI onboard Sentinel-5 Precursor,
     Atmospheric Measurement Techniques, 12, 6771–6802, https://doi.org/10.5194/amt-12-6771-2019, 2019.

Schneising, O., Buchwitz, M., Hachmeister, J., Vanselow, S., Reuter, M., Buschmann, M., Bovensmann, H., and Burrows, J. P.: Advances in retrieving XCH$_4$ and XCO from Sentinel-5 Precursor: improvements in the scientific TROPOMI/WFMD algorithm, Atmospheric Measurement Techniques, 16, 669–694, https://doi.org/10.5194/amt-16-669-2023, 2023.

440 Seabold, S. and Perktold, J.: Statsmodels: Econometric and statistical modeling with python, in: Proceedings of the 9th Python in Science Conference, vol. 57, p. 61, Austin, TX, 2010.

Sierk, B., Fernandez, V., Bézy, J.-L., Meijer, Y., Durand, Y., Courrèges-Lacoste, G. B., Pachot, C., Löscher, A., Nett, H., Minoglou, K., et al.: The Copernicus CO2M mission for monitoring anthropogenic carbon dioxide emissions from space, in: International Conference on Space Optics—ICSO 2020, vol. 11852, pp. 1563–1580, SPIE, https://doi.org/10.1117/12.2599613, 2021.

445 Somkuti, P., O'Dell, C. W., Crowell, S., Köhler, P., McGarragh, G. R., Cronk, H. Q., and Burgh, E. B.: Solar-induced chlorophyll fluorescence from the Geostationary Carbon Cycle Observatory (GeoCarb): An extensive simulation study, Remote Sensing of Environment, 263, 112 565, https://doi.org/10.1016/j.rse.2021.112565, 2021.

Uieda, L., Tian, D., Leong, W. J., Schlitzer, W., Grund, M., Jones, M., Fröhlich, Y., Toney, L., Yao, J., Magen, Y., Tong, J.-H., Materna, K., Belem, A., Newton, T., Anant, A., Ziebarth, M., Quinn, J., and Wessel, P.: PyGMT: A Python interface for the Generic Mapping Tools,

450 https://doi.org/10.5281/zenodo.7772533, 2023.

Virtanen, P., Gommers, R., Oliphant, T. E., Haberland, M., Reddy, T., Cournapeau, D., Burovski, E., Peterson, P., Weckesser, W., Bright, J., et al.: SciPy 1.0: fundamental algorithms for scientific computing in Python, Nature methods, 17, 261–272, https://doi.org/10.1038/s41592-019-0686-2, 2020.

Wessel, P., Luis, J. F., Uieda, L., Scharroo, R., Wobbe, F., Smith, W. H. F., and Tian, D.: The Generic Mapping Tools Version 6, Geochemistry,

455 Geophysics, Geosystems, 20, 5556–5564, https://doi.org/10.1029/2019GC008515, 2019.

Wu, L., Hasekamp, O., Hu, H., Landgraf, J., Butz, A., Aben, I., Pollard, D. F., Griffith, D. W., Feist, D. G., Koshelev, D., et al.: Carbon dioxide retrieval from OCO-2 satellite observations using the RemoTeC algorithm and validation with TCCON measurements, Atmospheric Measurement Techniques, 11, 3111–3130, https://doi.org/10.5194/amt-11-3111-2018, 2018.

Wunch, D., Wennberg, P. O., Toon, G. C., Connor, B. J., Fisher, B., Osterman, G. B., Frankenberg, C., Mandrake, L., O'Dell, C., Ahonen, P.,

460 Biraud, S. C., Castano, R., Cressie, N., Crisp, D., Deutscher, N. M., Eldering, A., Fisher, M. L., Griffith, D. W. T., Gunson, M., Heikkinen, P., Keppel-Aleks, G., Kyrö, E., Lindenmaier, R., Macatangay, R., Mendonca, J., Messerschmidt, J., Miller, C. E., Morino, I., Notholt, J., Oyafuso, F. A., Rettinger, M., Robinson, J., Roehl, C. M., Salawitch, R. J., Sherlock, V., Strong, K., Sussmann, R., Tanaka, T., Thompson, D. R., Uchino, O., Warneke, T., and Wofsy, S. C.: A method for evaluating bias in global measurements of CO$_2$ total columns from space, Atmospheric Chemistry and Physics, 11, 12 317–12 337, https://doi.org/10.5194/acp-11-12317-2011, 2011.

465 Young, A. H., Knapp, K. R., Inamdar, A., Hankins, W., and Rossow, W. B.: The international satellite cloud climatology project H-Series climate data record product, Earth System Science Data, 10, 583–593, https://doi.org/10.5194/essd-10-583-2018, 2018.